Isogeometric shape optimization of smoothed petal auxetic structures via computational periodic homogenization

Zhen-Pei Wang[a], Leong Hien Poh[a,*], Justin Dirrenberger[b], Yilin Zhu[a], Samuel Forest[c]

[a] *Department of Civil and Environmental Engineering, National University of Singapore 1 Engineering Drive 2, E1A 07-03 Singapore 117576, Singapore*
[b] *Laboratoire PIMM, Ensam, CNRS, Cnam, Hesam Université, 151 bd de l'Hôpital, 75013 Paris, France*
[c] *Centre des Matériaux, MINES-ParisTech, CNRS UMR 7633, BP 87, 91 003 Evry Cedex, France*

Abstract

An important feature that drives the auxetic behaviour of the star-shaped auxetic structures is the hinge-functional connection at the vertex connections. This feature poses a great challenge for manufacturing and may lead to significant stress concentrations. To overcome these problems, we introduced smoothed petal-shaped auxetic structures, where the hinges are replaced by smoothed connections. To accommodate the curved features of the petal-shaped auxetics, a parametrisation modelling scheme using multiple NURBS patches is proposed. Next, an integrated shape design frame work using isogeometric analysis is adopted to improve the structural performance. To ensure a minimum thickness for each member, a geometry sizing constraint is imposed via piece-wise bounding polynomials. This geometry sizing constraint, in the context of isogeometric shape optimization, is particularly interesting due to the non-interpolatory nature of NURBS basis. The effective Poisson ratio is used directly as the objective function, and an adjoint sensitivity analysis is carried out. The optimized designs – smoothed petal auxetic structures – are shown to achieve low negative Poisson's ratios, while the difficulties of manufacturing the hinges are avoided. For the case with six petals, an in-plane isotropy is achieved.

1. Introduction

In contrast to conventional materials that contract (expand) transversely when stretched (compressed), auxetic materials expand (contract) perpendicularly to the stretching (compression) direction, leading to a so-called negative Poisson's ratio (NPR). This auxetic behaviour leads to interesting performance in energy absorption, shear, indentation, damping, acoustics and crushing, with many potential applications in the civil and military sectors [1–7].

---

* Corresponding author.
   E-mail address: leonghien@nus.edu.sg (L.H. Poh).
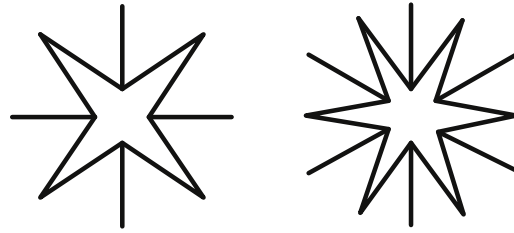
Fig. 1. Star-shaped structures with 4 and 6 vertices [40,41,6].

The design of auxetic (micro-) structures has attracted research interests for more than three decades. In 1985, Almgren presented a structure with Poisson's ratio of −1 using rods, hinges, and springs [8]. Conceptual designs of composite materials with Poisson's ratio close to −1 were presented in [9]. Some important features of auxetic materials, such as the re-entrant corners, were discussed in the works of Lakes [10], Friis et al. [11], Evans [12], and Phan-Thien and Karihaloo [13]. A separate class of 3D auxetics that exploits the buckling mechanism in structures is proposed by [14]. Design techniques using modern numerical methods such as topology optimization started with the work of Sigmund [15], in which a topology optimization framework for designing 2D and 3D auxetic truss-based structures was presented. The work was next extended into a 2D continuum-based approach in [16] and further developed into a manufacturable compliant micro-mechanism with negative Poisson's ratio in [17].

Since these pioneering work, different techniques have been adopted for auxetic structure design optimization. Radman [18] studied the topology design for auxetic structures using bi-directional evolutionary structural optimization (BESO) method [19–21]. Wang and co-workers [22,23] presented some design optimization works using level-set method [24–26]. Schwerdtfeger et al. [27] utilized topology optimization to improve a given 3D auxetic structure, such that the resulting design is acceptable for the manufacturing process. Kureta and Kanno [28] studied the auxetic structure design using a mixed integer programming approach. Kaminakis and Stavroulakis [29] presented an evolutionary-hybrid algorithm to perform the design optimization. Using genetic algorithm and differential evolutionary algorithm, a unit cell of disordered rib grids-based structures is optimized to achieve a negative Poisson ratio in the works of Javadi et al. [30] and Horrigan et al. [31]. Isotropic design optimization for auxetic material is studied recently by Czarnecki and Wawruch [32]. Recent efforts incorporating geometrical non-linearity and manufacturability constraint in the design optimization can be found in the works of Wang et al. [33] and Clausen et al. [34], with the resulting structures having high geometrical simplicity, design flexibility, and manufacturability. Other design techniques for molecular structures and multi-scale problems can be found in [35–39].

In this paper, we focus on the class of star-shaped auxetic structures depicted in Fig. 1, which has been studied by several researchers [e.g. [40–42]]. Generally, the auxetic performance of a star-shaped structure is dependent on the flexibility at the vertices. Hinge-like connections, while beneficial, cannot be manufactured easily. Continuous vertices are amenable to the manufacturing process, though the sharp corners induce a stress concentration effect. Moreover, the rigidity of connections at vertices degrade the auxetic performance of a star-shaped structure, to be discussed later in Section 2.

Following this concept, we propose a series of smoothed petal conceptual designs, examples as shown in Fig. 2, based on the smoothening of connections in the reference star-shaped structures. With an appropriate shape design technique, a reasonably good auxetic behaviour of these conceptual designs can be achieved, without the manufacturing difficulties associated with hinge-like connections.

A key challenge for the shape design of the proposed smoothed petal structures is the proper integration between the curved geometrical description and the corresponding finite element analysis. Using non-uniform rational b-spline (NURBS) basis function as the shape function, the isogeometric analysis (IGA) [43] is well suited for shape optimization in terms of the exact geometrical description and enhanced sensitivity analysis [44,45]. Shape optimization based IGA has been adopted for curved beam structures [46,47], vibrating membranes [48], fluid mechanics [49], shells [50,51], photonic crystals [52], Stokes flow problems [53], etc. Other works using NURBS as a tool for shape optimization can be found in [54–57].

Shape optimization has been utilized for the design of auxetics [e.g. [33,34]]. Departing from these established approaches, this paper adopts isogeometric analysis for shape design optimization of auxetic structures such that
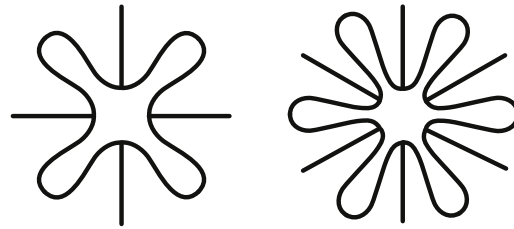
Fig. 2. New conceptual petal-shaped structures design with 4 and 6 petals.

the curved features of the geometry can be naturally preserved. For practical engineering considerations, a geometry sizing constraint is introduced to ensure a minimum thickness, such that thin member connections do not surface. This geometry sizing constraint is difficult to implement in the context of isogeometric analysis due to the non-interpolatory nature of NURBS basis, which makes it a particularly interesting problem to solve.

In general, the effective elastic properties of a periodic architectured material are not isotropic [58–61]. It is therefore essential to determine the full effective elastic modulus tensor for a given structure. This is done in the present work by means of computational homogenization [62], with periodic boundary conditions applied on the unit cell and the associated boundary value problem resolved [63]. As a special case, we consider in this paper a smoothed petal shape design with 6-fold symmetry to achieve in-plane isotropy, thus contributing to the pool of isotropic designs in the literature [e.g. [17]].

The paper is organized as follows: The hinge effect in the reference star-shaped structures, and the motivation towards smoothed, manufacturable complaint connections is briefly discussed in Section 2. The problem statement and formulations including the design parametrisation, the numerical homogenization for the effective property, the design objective and its continuous adjoint sensitivity analysis are presented in Section 3. A brief introduction of IGA and the isogeometric discretization of the sensitivity analysis are presented in Section 4. Geometry constraints, including symmetry and sizing considerations in the framework of isogeometric shape optimization, are elaborated in Section 5. A simple descent iteration optimization algorithm is provided in Section 6. Numerical studies are implemented in Section 7, for the designs of smoothed tetra-petals and hexa-petals auxetic unit cells. Finally, some concluding remarks are summarized in Section 8.

In this paper, the dot (inner) product of two vectors (a, b) and two second-order tensors (A, B) are denoted as $a^{\mathrm{T}}b$ or $a \cdot b$ and $A \cdot B$, respectively. The product of a second-order tensor A and a vector b is denoted as Ab. The product of two second-order tensors is denoted as AB. The tensor product of two vectors is denoted as $a \otimes b$. To facilitate implementation, Voigt's notation is used in the formulations. A function f with its arguments # is written as $f[\#]$.

2. Smoothed and manufacturable hinge-type vertices

In the literature such as [40,41], star-shaped structures are mostly modelled using truss or beam elements with the vertices treated as hinges or hinging springs. While these hinges or hinging springs are the underlying mechanisms leading to the auxetic behaviour, they are not amenable for the manufacturing process. A more desirable approach for manufacturing is to have a continuous unit cell structure, an example of which is depicted in Fig. 3(a) for a star-shaped structure with four vertices presented in [40]. Considering an isotropic elastic material ($E = 1$; $v = 0.3$) with a unit member width, as shown in Fig. 3(a), an effective Poisson ratio of -0.144 is obtained. When subjected to a unity relative horizontal displacement, the deformed structure is plotted in Fig. 3(b) with the corresponding von Mises stress distribution. It is easily observed that the auxetic behaviour is limited, with severe stress concentration at the connections.

For a slightly modified star-shaped structure shown in Fig. 3(c) with smoothed vertices coupled with a reduced width, an effective Poisson ratio of -0.5365 is obtained. Applying the same boundary conditions for the modified structure, its auxetic behaviour is improved, and stress concentration at connections reduced, as illustrated in Fig. 3(c). Comparing the auxetic behaviour of these two designs, it is clear that a compliant connection at the vertices can mimic the hinge effect. This sets the backdrop for the following sections, where a proposed shape optimization technique is utilized on a reference geometry with smooth connections, for the design of manufacturable auxetic structures.
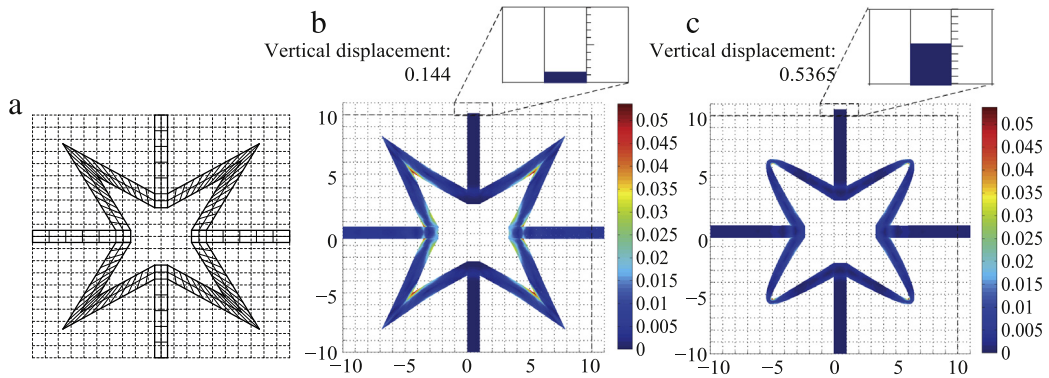
Fig. 3. (a) Star-shaped model from [40] built as a continuum with a width of 1. (b) The von Mises stress distribution of the star-shaped structure under a displacement of 1 applied to the right side. (c) The von Mises stress distribution of the modified star-shaped structure under a displacement of 1 applied to the right side.

3. Problem statement and formulation

3.1. Initial shape setting and shape updating scheme

Starting from a reference petal-shaped structure, we seek an optimized shape which maximizes its auxetic property. To simplify the design problem, we consider only the exterior boundary of one petal, termed *parent petal* hereinafter, since the entire structure can be obtained through the patterning of parent petal and addition of connecting bars. Correspondingly, the control points characterizing the exterior boundary of the parent petal are chosen as design variables.

The characterization of the initial parent petal begins with the definition of its interior boundary, as shown in Fig. 4(a). Practical manufacturing and engineering requirements, such as the maximum curvature and smoothness of the interior boundary, the minimum gap between the two arms, the number and size of petals must be taken into account. The curvature in the structure design affects the manufacturing accuracy [33] and the stress distribution. Therefore, the maximum curvature is a design requirement for some manufacturing methods and engineering performance. A minimal gap between the two arms is specified to avoid possible contact at small compressive strains. For a design with m petals, the angle θ is given by $2\pi/m$. To ensure a smooth connection between two adjacent petals, the tangents of the two ends are required to be perpendicular to the symmetry line (the dash lines along angle θ). The interior boundary of the parent petal is fixed during the design process, such that requirements for maximum curvature and minimum gap between the two arms can be maintained during the optimization process.

Next, the initial exterior boundary of the parent petal, i.e., the initial design boundary with its corresponding control points as design variables, is obtained via a simple offset of the control points for the interior boundary (see Fig. 4(b)). The interior and exterior boundaries are connected via straight lines at the planes of symmetry, which forms a closed boundary for one petal. Next, the petal is translated vertically with a distance depending on the size of the connecting bars, as illustrated in Fig. 4(c). The space where the parent petal is defined is called *design space* hereinafter. Finally, by patterning the parent petal in a circular direction, with the insertion of connecting bars, a full model of a unit-cell can be generated (see Fig. 4(d)). For a control point $\boldsymbol{x}^{P0}$ of the parent petal in the design space, the corresponding control point $\boldsymbol{x}^{Pi}$ of the ith petal is evaluated using
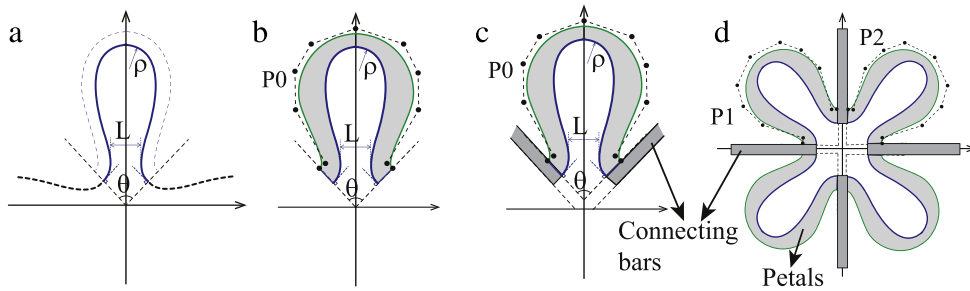
$$\boldsymbol{x}^{Pi} = \boldsymbol{T}\boldsymbol{x}^{P0}, \tag{1}$$

where $\boldsymbol{T}$ is a rotation matrix defined as

$$\boldsymbol{T} = \begin{bmatrix} \cos\vartheta & -\sin\vartheta \\ \sin\vartheta & \cos\vartheta \end{bmatrix}, \tag{2}$$

with ϑ as the rotation angle.

During the iterative design process, the full unit cell model is updated according to the following procedure. First, a numerical homogenization is performed on the full unit cell to compute the effective Poisson ratio and other required

Fig. 4. (a) Characterization of the interior boundary of the parent petal. (b) Generating initial exterior boundary of the parent petal. (c) Translation of the parent petal in the design space. (d) Patterning the parent petal and inserting the connecting bars to generate the full model.
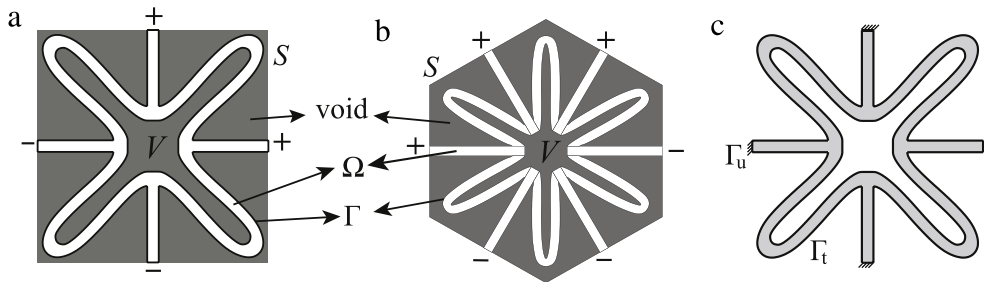
Fig. 5. The RVE of a smoothed (a) tetra-petal structure and (b) hexa-petal structure. (c) The displacement and traction boundaries, $\Gamma = \Gamma_u + \Gamma_t$.

structural response for shape sensitivity analysis. Next, an adjoint model is numerically implemented such that the shape sensitivity analysis, with respect to the design control points of half the number of petals of a full unit, can be evaluated. The shape sensitivity is then inversely rotated back to the design space using $\boldsymbol{T}^{-1}$, such that the shape of the parent petal can be updated (details presented in Sections 5 and 6). Finally, a new full model is updated based on the current parent petal.

3.2. Effective elastic properties with computational homogenization method

The effective material properties of an auxetic design can be obtained through the numerical homogenization of a representative volume element (RVE) occupied in domain V with boundary S, as depicted in Fig. 5. In the following, we term the fine scale analysis within a RVE as *micro*, and the coarse engineering scale as *macro*.

Within a RVE, the bulk material forming the structure occupies a sub-domain $\Omega \subset V$ with boundary Γ. This structure characterized by region Ω is the design object, while the rest of the RVE is empty (void). The updated designs of region Ω in an iterative design process, can be treated as a sequence that follows a time-like parameter τ. In analogy to the configuration transformation with time in continuum mechanics [64,65], this time-like parameter τ is used to represent the sequential designs, i.e., the design domain at τ is termed Ω^τ with boundary Γ^τ, and the location of an arbitrary material point $\boldsymbol{p}$ is defined as $\boldsymbol{x}[\boldsymbol{p}, \tau]$.

Imposing the periodic boundary conditions with a given macro strain $\boldsymbol{E}$ on the structure occupied in Ω^τ, a boundary value problem can be obtained for the micro-scale structure as

$$\begin{cases} \boldsymbol{c}[\boldsymbol{u}] := \operatorname{div} \boldsymbol{\sigma} = \operatorname{div}(\mathbb{C}\nabla\boldsymbol{u}) = \boldsymbol{0} & \text{in } \Omega^\tau \\ \hat{\boldsymbol{t}} = \boldsymbol{0} & \text{on } \Gamma_t^\tau \\ \boldsymbol{u}^+ - \boldsymbol{u}^- = \boldsymbol{E}(\boldsymbol{x}^+ - \boldsymbol{x}^-) & \text{on } \Gamma_u^\tau \end{cases} \tag{3}$$

where $\mathbb{C}$ denotes the elasticity tensor of the bulk material property, the symbols '$+$' and '$-$' denote the opposing sides of a RVE, and ∇ is the gradient operator. Solving this boundary value problem, the macro stress can be obtained as

$$\boldsymbol{\Sigma} = \frac{1}{V} \int_{\Omega^\tau} \boldsymbol{\sigma} \, d\Omega. \tag{4}$$

Following this, the homogenized elasticity tensor $\bar{\mathbb{C}}$ can be obtained using the relation

$$\boldsymbol{\Sigma} = \bar{\mathbb{C}}\boldsymbol{E}. \tag{5}$$

For simplicity, we consider orthotropic effective media in plane stress. The homogenized elasticity tensor is given as

$$\begin{bmatrix} \Sigma_{11} \\ \Sigma_{22} \\ \Sigma_{12} \end{bmatrix} = \begin{bmatrix} Q_{11} & \bar{v}_{21}Q_{11} & 0 \\ \bar{v}_{21}Q_{11} & Q_{22} & 0 \\ 0 & 0 & Q_{66} \end{bmatrix} \begin{bmatrix} E_{11} \\ E_{22} \\ 2E_{12} \end{bmatrix}, \tag{6}$$

where $\bar{v}_{ij}$ denotes the effective Poisson ratio in direction x_j that is orthogonal to the stretched direction x_i. For a given effective Young modulus E_i^Y in the x_i direction, and an effective shear modulus G_{ij} in the $x_i - x_j$ plane, the components Q_{ij} can be written as

$$Q_{11} = \frac{E_1^Y}{1 - \bar{v}_{12}\bar{v}_{21}}, \quad Q_{22} = \frac{E_2^Y}{1 - \bar{v}_{12}\bar{v}_{21}}, \quad \text{and } Q_{66} = G_{12}.$$

Note that

$$E_1^Y \bar{v}_{21} = E_2^Y \bar{v}_{12}, \tag{7}$$

for a macro strain $\boldsymbol{E} = [1, \ 0, \ 0]^T$ and applying the corresponding periodic boundary conditions, the effective Poisson ratio $\bar{v}_{21}$ can be easily determined from Eqs. (6) and (7) as

$$\bar{v}_{21} = \frac{\Sigma_{22}}{\Sigma_{11}} = \frac{\int_{\Omega^\tau} \sigma_{22} d\Omega}{\int_{\Omega^\tau} \sigma_{11} d\Omega}. \tag{8}$$

Similarly, for a macro strain $\boldsymbol{E} = [0, \ 1, \ 0]^T$ and applying the corresponding periodic boundary conditions, the effective Poisson ratio $\bar{v}_{12}$ can be determined as

$$\bar{v}_{12} = \frac{\Sigma_{11}}{\Sigma_{22}} = \frac{\int_{\Omega^\tau} \sigma_{11} d\Omega}{\int_{\Omega^\tau} \sigma_{22} d\Omega}. \tag{9}$$

3.3. Design objective and sensitivity analysis

The problem statement is to find the optimized shape of the design boundary, such that the effective negative Poisson ratio is minimized. For the petal-shaped designs depicted in Fig. 2, we seek to preserve the geometrical symmetry about x_1 and x_2 during the optimization process – to be elaborated later in Section 5 – such that $\bar{v}_{21} = \bar{v}_{12}$. Accordingly, the objective function can be defined as the minimization of the effective Poisson ratio solely in terms of $\bar{v}_{21}$ in Eq. (8), i.e. for a macro strain of $\boldsymbol{E} = [1, \ 0, \ 0]^T$,

$$\Phi := \bar{v}_{21} = \frac{\int_{\Omega^\tau} \sigma_{22} d\Omega}{\int_{\Omega^\tau} \sigma_{11} d\Omega}. \tag{10}$$

The shape gradient with respect to the design parameter τ can be derived using the adjoint method, the basic idea of which follows the Lagrangian multiplier approach [65]. Given the objective function in Eq. (10), in order to satisfy the equality constraints from the equilibrium condition in Eq. (3) at any point $\boldsymbol{x} \in \Omega^\tau$, an augmented functional is introduced as

$$\tilde{\Phi} = \Phi + \langle \boldsymbol{c}[\boldsymbol{u}], \boldsymbol{u}^* \rangle_{\Omega^\tau} \tag{11}$$

where

$$\langle \boldsymbol{c}[\boldsymbol{u}], \boldsymbol{u}^* \rangle_{\Omega^\tau} = \int_{\Omega^\tau} \boldsymbol{u}^* \cdot (\operatorname{div} \mathbb{C}\nabla\boldsymbol{u}) d\Omega = -\int_{\Omega^\tau} \nabla\boldsymbol{u}^* \cdot (\mathbb{C}\nabla\boldsymbol{u}) d\Omega + \int_{\Gamma^\tau} \boldsymbol{t} \cdot \boldsymbol{u}^* d\Gamma. \tag{12}$$

The Lagrangian multiplier $\boldsymbol{u}^*$ is the so called adjoint displacement field and $\boldsymbol{t}$ is the traction on boundary Γ^τ. Recalling that $\hat{\boldsymbol{t}} = \boldsymbol{0}$ on Γ_t^τ, we have

$$\langle \boldsymbol{c}[\boldsymbol{u}], \boldsymbol{u}^* \rangle_{\Omega^\tau} = -\int_{\Omega^\tau} \nabla\boldsymbol{u}^* \cdot (\mathbb{C}\nabla\boldsymbol{u}) d\Omega + \int_{\Gamma_u^\tau} \boldsymbol{t} \cdot \boldsymbol{u}^* d\Gamma. \tag{13}$$

The next step is to derive the total derivative of Eq. (11) with respect to design parameter τ

$$\overset{\circ}{\tilde{\Phi}} = \frac{D\tilde{\Phi}}{D\tau} = \overset{\circ}{\Phi} + \frac{D}{D\tau}\langle c[u], u^*\rangle_{\Omega^\tau}, \tag{14}$$

where $(\overset{\circ}{\cdot}) = \frac{D(\cdot)}{D\tau}$ represents the *total* or *material design* derivative.

Given a continuous differentiable function h defined in Ω^τ and Γ^τ, the volume and surface transport relations are expressed, respectively, as

$$\frac{D}{D\tau} \int_{\Omega^\tau} h d\Omega = \int_{\Omega^\tau} h' d\Omega + \int_{\Gamma^\tau} h v_n d\Gamma \tag{15}$$

and

$$\frac{D}{D\tau} \int_{\Gamma^\tau} h d\Gamma = \int_{\Gamma^\tau} (h' + \nabla h \cdot \boldsymbol{n} v_n - \kappa h v_n) d\Gamma, \tag{16}$$

where the notation $(\cdot)'$ denotes the *partial* or *spatial design* derivatives, κ is the total curvature [66], $\boldsymbol{v}$ is the so-called design velocity at $\boldsymbol{x}$,

$$\boldsymbol{v} := \overset{\circ}{\boldsymbol{x}} = \frac{D\boldsymbol{x}}{D\tau}, \tag{17}$$

and $v_n = \boldsymbol{v} \cdot \boldsymbol{n}$.

Using the transport relation Eq. (15) and bearing in mind that $\int_{\Omega^\tau} \sigma_{ij} d\Omega = V\Sigma_{ij}$, the first term on the right side of Eq. (14) can be written as

$$\overset{\circ}{\Phi} = \frac{1}{V\Sigma_{11}} \frac{D}{D\tau} \int_{\Omega^\tau} \sigma_{22} d\Omega - \frac{\Sigma_{22}}{V\Sigma_{11}^2} \frac{D}{D\tau} \int_{\Omega^\tau} \sigma_{11} d\Omega \tag{18}$$

in which

$$\frac{D}{D\tau} \int_{\Omega^\tau} \sigma_{11} d\Omega = \int_{\Omega^\tau} (\sigma_{11,\sigma} \boldsymbol{\sigma}_{,u}) \cdot \boldsymbol{u}' d\Omega + \int_{\Gamma^\tau} \sigma_{11} \boldsymbol{v} \cdot \boldsymbol{n} d\Gamma \tag{19}$$

and

$$\frac{D}{D\tau} \int_{\Omega^\tau} \sigma_{22} d\Omega = \int_{\Omega^\tau} (\sigma_{22,\sigma} \boldsymbol{\sigma}_{,u}) \cdot \boldsymbol{u}' d\Omega + \int_{\Gamma^\tau} \sigma_{22} \boldsymbol{v} \cdot \boldsymbol{n} d\Gamma. \tag{20}$$

Note that the spatial gradient operation $\nabla \boldsymbol{u}$ and the design derivative $\boldsymbol{u}'$ commute, such that $\boldsymbol{\sigma}'[\boldsymbol{u}] = \boldsymbol{\sigma}_{,u} \cdot \boldsymbol{u}' = \boldsymbol{\sigma}[\boldsymbol{u}'] = \mathbb{C}\nabla\boldsymbol{u}'$. Following this and substituting Eqs. (20) and (19) into Eq. (18), we obtain

$$\overset{\circ}{\Phi} = \int_{\Omega^\tau} \boldsymbol{\varepsilon}^* \mathbb{C}\nabla\boldsymbol{u}' d\Omega + \int_{\Gamma^\tau} \alpha \boldsymbol{v} \cdot \boldsymbol{n} d\Gamma, \tag{21}$$

in which $\boldsymbol{\varepsilon}^*$ is the adjoint initial strain defined as

$$\boldsymbol{\varepsilon}^* = \left\{ -\frac{\Sigma_{22}}{V\Sigma_{11}^2}, \frac{1}{V\Sigma_{11}}, 0 \right\}^T = \frac{1}{V\Sigma_{11}}\{-\bar{v}_{21}, 1, 0\}^T, \tag{22}$$

and

$$\alpha = \frac{1}{V\Sigma_{11}}\sigma_{22} - \frac{\Sigma_{22}}{V\Sigma_{11}^2}\sigma_{11}. \tag{23}$$

Similarly, using the transport relations defined in Eqs. (15) and (16), the derivative of the second term on the right side of Eq. (11) is derived as

$$\frac{D}{D\tau}\langle c[u], u^*\rangle_{\Omega^\tau} = -\int_{\Omega^\tau} \mathbb{C}\nabla\boldsymbol{u}' \cdot \nabla\boldsymbol{u}^* d\Omega - \int_{\Gamma^\tau} \mathbb{C}\nabla\boldsymbol{u} \cdot \nabla\boldsymbol{u}^* (\boldsymbol{v} \cdot \boldsymbol{n}) d\Gamma$$
$$+ \int_{\Gamma_u^\tau} \left(\boldsymbol{t}' \cdot \boldsymbol{u}^* + \nabla (\boldsymbol{t} \cdot \boldsymbol{u}^*) \cdot \boldsymbol{n} v_n - \kappa (\boldsymbol{t} \cdot \boldsymbol{u}^*) v_n \right) d\Gamma, \tag{24}$$

where terms involving $\boldsymbol{u}*'$ vanish by considering $\langle c[u], u^{*'}\rangle_{\Omega^\tau} = 0$.

Utilizing Eqs. (21) and (24), Eq. (14) can be rewritten as

$$\overset{\circ}{\tilde{\Phi}} = \Psi_1 + \Psi_2, \tag{25}$$

where

$$\Psi_1 = \int_{\Omega^\tau} \boldsymbol{\varepsilon}^* \cdot \mathbb{C}\nabla\boldsymbol{u}' \mathrm{d}\Omega - \int_{\Omega^\tau} \mathbb{C}\nabla\boldsymbol{u}' \cdot \nabla\boldsymbol{u}^* \mathrm{d}\Omega + \int_{\Gamma^\tau} \boldsymbol{t}' \cdot \boldsymbol{u}^* \mathrm{d}\Gamma$$
$$= \int_{\Omega^\tau} \mathrm{div}\left(\mathbb{C}(\nabla\boldsymbol{u}^* - \boldsymbol{\varepsilon}^*)\right) \cdot \boldsymbol{u}' \mathrm{d}\Omega + \int_{\Gamma^\tau} \left(\mathbb{C}(\boldsymbol{\varepsilon}^* - \nabla\boldsymbol{u}^*)\right)\boldsymbol{n} \cdot \boldsymbol{u}' \mathrm{d}\Gamma + \int_{\Gamma_u^\tau} \boldsymbol{t}' \cdot \boldsymbol{u}^* \mathrm{d}\Gamma \tag{26}$$

and

$$\Psi_2 = \int_{\Gamma^\tau} \left(\alpha - \mathbb{C}\nabla\boldsymbol{u} \cdot \nabla\boldsymbol{u}^*\right)v_n \,\mathrm{d}\Gamma + \int_{\Gamma_u^\tau} \left(\nabla\left(\boldsymbol{t} \cdot \boldsymbol{u}^*\right) \cdot \boldsymbol{n} - \kappa\left(\boldsymbol{t} \cdot \boldsymbol{u}^*\right)\right)v_n \,\mathrm{d}\Gamma. \tag{27}$$

In order to eliminate the implicitly dependent terms $\boldsymbol{u}'$ and $\boldsymbol{t}'$ in Eq. (26), a displacement-based adjoint model with no traction load is introduced such that

$$\begin{cases} \boldsymbol{c}^*[\boldsymbol{u}^*] := \mathrm{div}\,\mathbb{C}(\nabla\boldsymbol{u}^* - \boldsymbol{\varepsilon}^*) = \boldsymbol{0} & \text{in } \Omega^\tau \\ \hat{\boldsymbol{t}}^* = \left(\mathbb{C}(\boldsymbol{\varepsilon}^* - \nabla\boldsymbol{u}^*)\right)\boldsymbol{n} = \boldsymbol{0} & \text{on } \Gamma_t^\tau \\ \boldsymbol{u}^{*+} = \boldsymbol{u}^{*-} & \text{on } \Gamma_u^\tau \end{cases} \tag{28}$$

in which $\hat{\boldsymbol{t}}^*$ is the prescribed adjoint traction, respectively, and $\Gamma^\tau = \Gamma_u^\tau + \Gamma_t^\tau$. Utilizing the adjoint model, the equations reduce to

$$\Psi_1 = \int_{\Gamma_u^\tau} \left(\mathbb{C}(\boldsymbol{\varepsilon}^* - \nabla\boldsymbol{u}^*)\right)\boldsymbol{n} \cdot \boldsymbol{u}' \,\mathrm{d}\Gamma = \int_{\Gamma_u^\tau} \boldsymbol{t}^* \cdot \boldsymbol{u}' \,\mathrm{d}\Gamma \tag{29}$$

and

$$\Psi_2 = \int_{\Gamma^\tau} \left(\alpha - \mathbb{C}\nabla\boldsymbol{u} \cdot \nabla\boldsymbol{u}^*\right)v_n \,\mathrm{d}\Gamma. \tag{30}$$

Considering that the periodic boundary condition leads to $\boldsymbol{t}^{*+} = -\boldsymbol{t}^{*-}$, we have $\Psi_1 = 0$. In addition, observing that the design velocity $\boldsymbol{v}$ is non-vanishing only on the design boundary Γ_d^τ, the adjoint shape gradient of Eq. (11) can be simplified to give

$$\frac{\mathrm{D}}{\mathrm{D}\tau}\tilde{\Phi} = \int_{\Gamma_d^\tau} \left(\alpha - \mathbb{C}\nabla\boldsymbol{u} \cdot \nabla\boldsymbol{u}^*\right)(\boldsymbol{v} \cdot \boldsymbol{n}) \,\mathrm{d}\Gamma. \tag{31}$$

Alternatively, if ν_{12} is adopted as the design objective in (10) according to Eq. (9), the derivation of its shape gradient runs parallel to the above equations, and will not be repeated here. Note that the sensitivity analysis in this paper involves only the effective Poisson ratio. In cases where several effective material properties are involved in the sensitivity analysis, it is recommended to use the methodology presented in [15,16]. By considering the superposition of primary pre-strain loading cases for homogenization, the requirement of solving adjoint problems to obtain the sensitivity of different effective material properties is avoided.

4. Isogeometric discretization

The NURBS have been used as a tool to describe and design geometry for decades. The combination of the basis function defined in the index space, and the control points located in the physical space, offers great flexibility in CAD modelling. Using the basis functions as the shape functions for finite element analysis, isogeometric analysis integrates the CAE and CAD processes into one discretization scheme. The isogeometric shape optimization, which adopts the locations and weights of the control points as design variables, is naturally developed based on this integration between the two processes.

For the design of the smoothed petal auxetic structures proposed in this paper, an isogeometric shape optimization framework is well suited, since

- NURBS offer great flexibility and convenience in describing the geometry of the curved and smoothed petal auxetic structures;
- The curved geometry of the petal auxetic structure can be preserved exactly in the analysis, such that numerical errors are reduced;
- Less degrees of freedom are required for the analysis compared to the finite element discretization of the curved geometry associated with a smoothed petal auxetic.

4.1. NURBS-based isogeometric analysis

A general expression for a NURBS curve with parameter ξ is written as

$$x[\xi] = \sum_{i=1}^{n} R^{i,p}[\xi]x^i = \sum_{i=1}^{n} \frac{N^{i,p}[\xi]w^i}{W[\xi]}x^i, \tag{32}$$

where n is the number of the control points x^i, p denotes the degree of the curve, $R^{i,p}$ and $N^{i,p}[\xi]$ are the basis functions, w^i is the weight of the ith control point, and $W[\xi] := \sum_{j=1}^{n} N^{j,p}[\xi]w^j$. Based on a non-decreasing knot vector $\boldsymbol{\xi} = \{\xi_1, \xi_2, \xi_3, \ldots, \xi_{n+p+1}\}$, expressions for the B-spline basis functions $N^{i,p}[\xi]$ can be defined following the Cox–de Boor recursion formula

$$N^{i,0}[\xi] = \begin{cases} 1 & \text{if } \xi_i \leqslant \xi < \xi_{i+1} \\ 0 & \text{otherwise} \end{cases}$$

$$N^{i,p}[\xi] = \frac{\xi - \xi_i}{\xi_{i+p} - \xi_i} N^{i,p-1}[\xi] + \frac{\xi_{i+p+1} - \xi}{\xi_{i+p+1} - \xi_{i+1}} N^{i+1,p-1}[\xi], \quad (p > 0). \tag{33}$$

Following Eq. (32), NURBS surfaces with parameters ξ and η are derived similarly as

$$x[\xi, \eta] = \sum_{i=1}^{n} \sum_{j=1}^{m} R^{ij}[\xi, \eta]x^{ij}. \tag{34}$$

It can be observed that the definitions of the NURBS geometry can be generally expressed as

$$x = \sum_I R^I[\boldsymbol{\chi}]x^I, \tag{35}$$

in which the index I and the parameter $\boldsymbol{\chi}$ are indicated in the following relation

$$R^I[\boldsymbol{\chi}] = \begin{cases} R^i[\xi], & \text{for 1D parametric space} \\ R^{ij}[\xi, \eta], & \text{for 2D parametric space.} \end{cases} \tag{36}$$

In an isogeometric analysis, the displacement fields are discretized using NURBS parametrisation as follows:

$$\boldsymbol{u} = \sum_I R^I \boldsymbol{u}^I, \tag{37}$$

where $\boldsymbol{u}^I$ is the displacement corresponding to the Ith control point. This representation is substituted into the weak formulation of a boundary value problem to obtain a system of equations assembled as

$$KU = F, \tag{38}$$

where K is the global stiffness matrix, U is the unknown displacement vector and F is the load vector.

4.2. Different discretizations in the design and analysis spaces

In the context of isogeometric shape optimization, the NURBS model can be discretized differently for efficient analysis and design, as schematically shown in Fig. 6. In the design space, the geometry is updated with a coarse discretization, in order to reduce the number of design variables. In the analysis space, a refined discretization is utilized such that the state fields and geometrical features can be computed accurately. The continuous shape sensitivity obtained in Eq. (31) is processed in both the design and the analysis spaces, i.e., the state variable fields and the geometrical features are calculated in the analysis space, while the design velocity $\boldsymbol{v}$ is discretized in the design space such that the shape sensitivity is obtained with respect to the design control points (see Section 4.3). The two levels of discretization can be achieved simply by inserting different numbers of knots in the NURBS index space.

4.3. Isogeometric shape design sensitivity analysis

Following Eq. (35), the design velocity can be expressed as

$$\boldsymbol{v} = \sum_I R^I[\boldsymbol{x}]\frac{d\boldsymbol{x}^I[\tau]}{d\tau}. \tag{39}$$

(a) Design discretization space.

(b) Analysis discretization space.

Fig. 6. Two levels NURBS discretizations: (a) Coarse discretization for design, (b) Refined discretization for analysis.
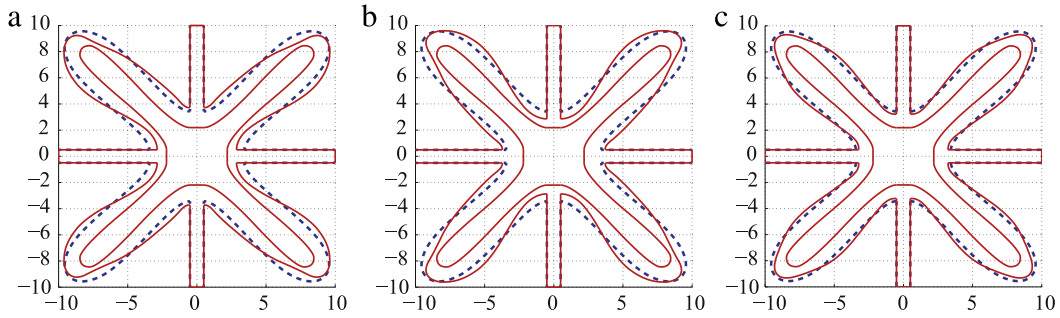

Fig. 7. (a) Shape updated using v_{21} as the design objective during the optimization process, resulting in $v_{21} = -1.3873$ and $v_{12} = -0.5989$; (b) Shape updated using v_{12} as the design objective during the optimization process, resulting in $v_{21} = -0.5989$ and $v_{12} = -1.3873$; (c) Shape updated using the modified gradient considering geometry symmetry, which is equivalent to double loading cases with both v_{21} and v_{12} considered, resulting in $v_{21} = v_{12} = -0.7889$.

Substituting Eq. (39) in Eq. (31), the discretized isogeometric shape gradient with respect to the design control point x^i can be obtained as

$$\Phi_{,x^I} = \frac{\partial \Phi}{\partial x^I} = \int_{\Gamma_d^{\mathfrak{r}}} R^I \Big(\alpha - \mathbb{C} \nabla u \cdot \nabla u^* \Big) n \, d\Gamma \ . \tag{40}$$

By solving for the unknown displacement fields u and u^* in the primary and adjoint problems, respectively, the discretized shape derivatives in Eq. (40) can be evaluated.

5. Geometry constraints

5.1. Symmetry constraint

Thus far, the proposed scheme is uni-directional in x_1 seeking the minimization of v_{21}, based on a macro strain $E = [1, \ 0, \ 0]^T$. We now refer to the tetra-petals auxetic design as an illustrative example. The current optimization scheme will result in a design with non-symmetric arms as shown in Fig. 7(a), leading to different auxetic behaviour in the two orthogonal directions. A similar design is obtained along the loading direction x_2, for a macro strain of $E = [0, \ 1, \ 0]^T$, as depicted in Fig. 7(b). An identical response in the two orthogonal directions $(x_1, \ x_2)$ can be obtained naturally by considering the two loading cases together in the design process, the result of which is shown in Fig. 7(c) with symmetry arms. This procedure, however, requires two loading cases and their corresponding adjoint problems to be considered. A more efficient approach is presented here, which requires only one loading case. The shape sensitivity with respect to the design control points of two neighbouring petals, as illustrated in Fig. 8, is first computed. Next, the shape gradient with respect to each design control point is inversely rotated back to the design space using (see Fig. 9)

$$\bar{\Phi}_{,x^{Pi}} = T^{-1} \Phi_{,x^{Pi}}, \quad i = 1, \ 2. \tag{41}$$

Finally, the symmetry constraint can be satisfied by using the following shape gradient with respect to the design control points of the parent petal in the design space:

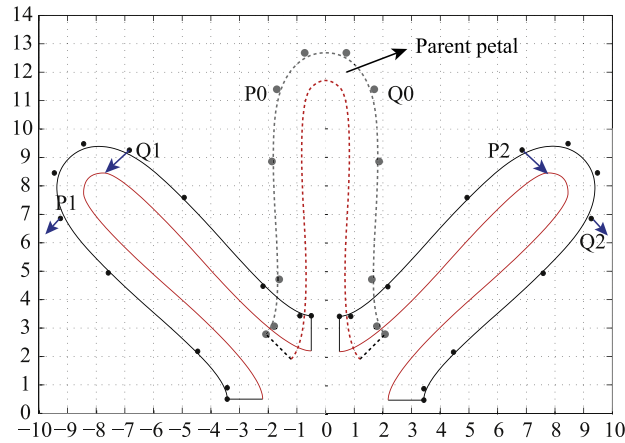$$\check{\Phi}_{,x^{P0}} = (\bar{\Phi}_{,x^{P1}} + \bar{\Phi}_{,x^{P2}})/2. \tag{42}$$

Fig. 8. Schematic location updating of the control points mapped from and of the parent petal for tetra-petals auxetic structures.
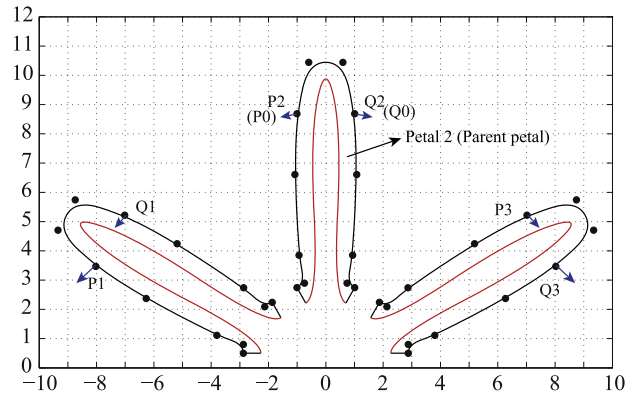

Fig. 9. Schematic location updating of the control points mapped from P0 and Q0 of the parent petal for hexa-petals auxetic structures.

Likewise, for the hexa-petals auxetic structure, the shape gradient with respect to the design control points for three neighbouring petals are calculated and inversely rotated back to the design space. The shape gradient with respect to the design control points of the parent petal in the design space is evaluated using

$$\check{\Phi}_{,x^{P0}} = (\bar{\Phi}_{,x^{P1}} + \bar{\Phi}_{,x^{P2}} + \bar{\Phi}_{,x^{P3}})/3. \tag{43}$$

5.2. Sizing constraint

The aforementioned symmetry constraint, by itself, may still result in an unsatisfactory design. Without any sizing control, the optimized shape will comprise of thin and weak connecting parts, as shown in Fig. 10(a), since the auxetic behaviour increases with the flexibility therewith. However, in practical engineering applications, these thin and weak connections are difficult to manufacture, and furthermore suffer from low loading capacity. Without any further treatments, some parts of the geometry may become too flimsy to fit standard engineering requirements. It is thus essential to introduce a sizing constraint that prevents the design from generating a part thinner than a given size. In a finite element based shape optimization analysis, this sizing constraint can be implemented simply by checking the distance between the nodes on the design boundary, and (interpolated) analogous points at the external boundary. For isogeometric shape optimization, however, the imposition of such a sizing constraint is challenging due to the (i) non-interpolatory property of NURBS and (ii) high computational cost involved in determining the distance between a point and a curved boundary. To overcome these challenges, a method using piece-wise bounding polynomial functions is proposed as follows:
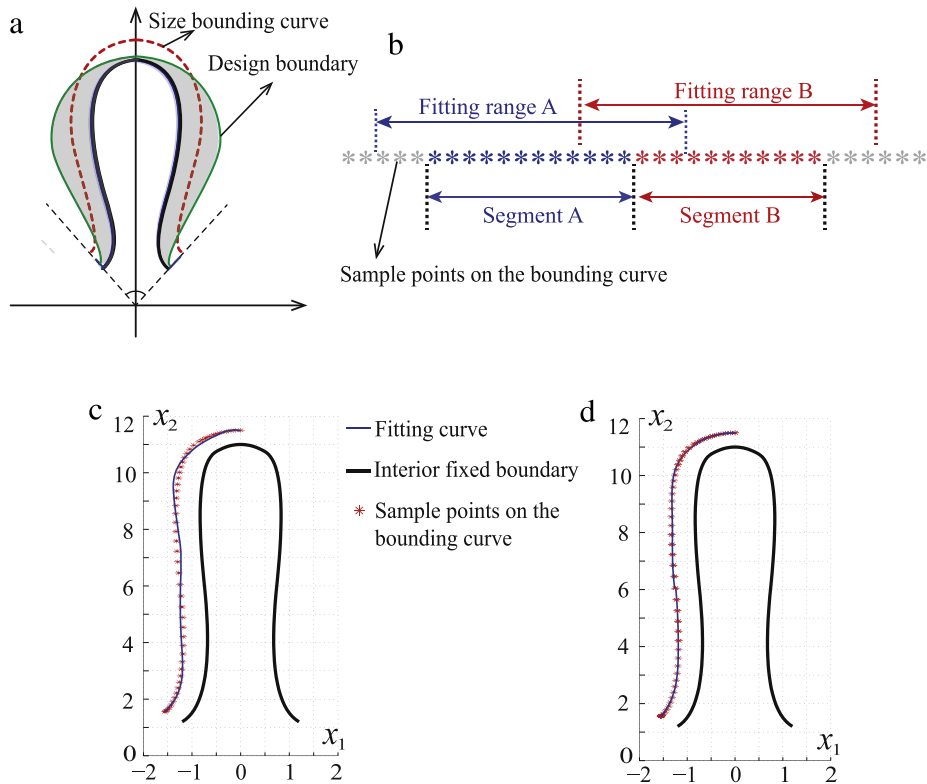
Fig. 10. (a) Illustration of the size bounding curve. (b) The piece-wise data fitting scheme. (c) Bounding curved fitted using one single polynomial of order 5: $f[\boldsymbol{x}] = x_1 - \sum_{i=0}^{5} a_i x_2^i$. (d) Bounding curve fitted using 4 piece-wise polynomials of order 5.

(1) A sufficiently large number of points on the interior fixed boundary are translated in the outward normal direction, with a magnitude given by the minimum thickness constraint. These translated sample points thus define the bounding curve, denoted by asterisk symbols in Figs. 6(b)–(d).

(2) After dividing the serial sample points into a few segments based on the distribution of the sample points, curve fitting tools can be used to generate a piece-wise bounding polynomial function $f[x_1, x_2]$. In this paper, the following function is utilized:

$$f[x_1, x_2] := x_1 - h[x_2], \quad \text{with} \quad h[x_2] = \sum_{i=0}^{5} a_i x_2^i. \tag{44}$$

For a geometrically simple bounding curve, e.g., a curve with small curvatures, a single polynomial might be sufficient. However, a bounding curve with complex geometry requires multiple piece-wise polynomials. For example, a closer fit to the bounding curve is observed in Fig. 10(d) with 4 segments compared to a single polynomial in Fig. 10(c) for the same function defined in Eq. (44). Due to symmetry, the sizing constraint is only evaluated on half a petal.

(3) To ensure a good fitting accuracy at the ends of each segment, it is necessary to do the data fitting over an extended range. For a segment corresponding to the sample points $[\boldsymbol{x}_i, \boldsymbol{x}_{i+1}, \ldots \boldsymbol{x}_j]$, the data fitting is to be done over the range $[\boldsymbol{x}_{i-k}, \boldsymbol{x}_{i-k+1}, \ldots, \boldsymbol{x}_i, \ldots, \boldsymbol{x}_j, \ldots, \boldsymbol{x}_{j+k}]$, where k is the number of the additional neighbour sample points to be utilized (see Fig. 10(b)).

(4) Once the bounding polynomial function $f[x_1, x_2]$ is ready, a point $\boldsymbol{x} = [x_1, x_2]$ located on the design boundary is checked against the sizing constraint via $f[x_1, x_2] < 0$. For the fitting polynomial Eq. (44) used in this paper, a point $\boldsymbol{x} = [x_1, x_2]$ with $f[x_1, x_2] < 0$ indicates that the point is located on the right of the bounding curve shown in Fig. 10(d), which violates the sizing constraint.
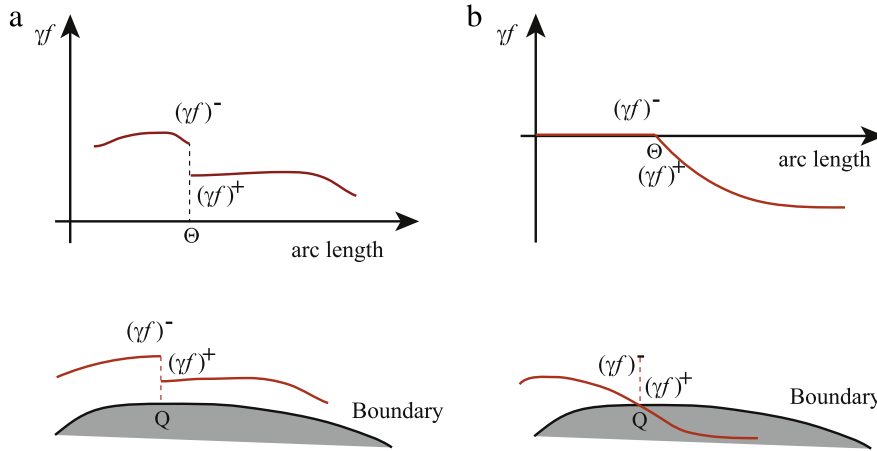
Fig. 11. Schematics of a 2D boundary integrand involving discontinuities.

(5) Introducing a function to quantify the violation of sizing constraint:

$$C := \int_{\Gamma_d^\tau} \gamma[\boldsymbol{x}] f[\boldsymbol{x}] \mathrm{d}\Gamma, \tag{45}$$

where Γ_d^τ is the design boundary and $\gamma[\boldsymbol{x}]$ is a penalty function at location $\boldsymbol{x}$ defined as

$$\gamma[\boldsymbol{x}] = \begin{cases} 1, & \text{sizing constraint violated, } f < 0 \\ 0, & \text{sizing constraint satisfied, } f \geqslant 0. \end{cases} \tag{46}$$

Using the boundary transport relation Eq. (16) and considering the discontinuities involved by introducing the penalty function $\gamma[\boldsymbol{x}]$, the total derivative of function C with respect to τ is

$$\frac{\mathrm{D}}{\mathrm{D}\tau} C = \int_{\Gamma_d^\tau} (f' + \nabla f \cdot \boldsymbol{n} - \kappa f)\gamma \boldsymbol{v} \cdot \boldsymbol{n} \mathrm{d}\Gamma + \int_\Theta [\![\gamma]\!] f \boldsymbol{m} \cdot \boldsymbol{v} \, \mathrm{d}\Theta, \tag{47}$$

where $[\![\cdot]\!] := (\cdot)^+ - (\cdot)^-$ represents a jump in the considered quantity at locations denoted by Θ, with $\boldsymbol{m}$ describing the tangential unit vectors along Θ (see [67] for details). This is illustrated schematically through a 2D boundary with a discontinuous field in Fig. 11(a).

The penalty function in Eq. (46) is in general, **discontinuous at the critical locations Θ where $f \neq 0$, see Fig. 11(b)**. However, the last term in Eq. (47) vanishes because $[\![\gamma]\!] f = (\gamma f)^+|_\Theta - (\gamma f)^-|_\Theta = 0$ at these critical locations. Together with the fact that the polynomial function f is independent of the design parameter τ, Eq. (47) reduces to

$$\frac{\mathrm{D}}{\mathrm{D}\tau} C = \int_{\Gamma_d^\tau} (\nabla f \cdot \boldsymbol{n} - \kappa f)\gamma \boldsymbol{v} \cdot \boldsymbol{n} \mathrm{d}\Gamma. \tag{48}$$

Following the same approach in Section 4.3 to discretize the design velocity $\boldsymbol{v}$, the discretized shape gradient of C with respect to the design control points is obtained as

$$C_{,\boldsymbol{x}^I} = \frac{\mathrm{D}}{\mathrm{D}\boldsymbol{x}^I} C = \int_{\Gamma_d^\tau} (\nabla f \cdot \boldsymbol{n} - \kappa f)\gamma \boldsymbol{n} R^I \mathrm{d}\Gamma. \tag{49}$$

Integrating the above shape gradients of the constraint and the objective functional for updating the locations of the design control points, an optimized solution satisfying the sizing constraint can be achieved using a proper iteration optimizer.

It is highlighted that this sizing constraint methodology can be extended to other isogeometric shape design cases where a fixed geometrical boundary is explicitly defined. However, in case that the interior petal boundary is not fixed, the presented sizing constraint cannot be directly adopted, and needs to be modified.

6. Iterative descent isogeometric optimization

Once the sensitivity analysis is numerically evaluated, the constrained optimization process can be carried out easily using different iteration optimizers. A crucial issue in the shape optimization process is the mesh quality. For the numerical examples used in paper, a relatively coarse mesh is used such that the mesh distortion caused by the adjacent control points overlapping during the shape updating is controllable. To ensure a balance movement of the boundary design control points, the following normalization approach is used [51,68]:

$$\hat{\Phi}_{,x^I} = \frac{\Phi_{,x^I}}{\int_{\Gamma_d^I} R^I \mathrm{d}\Gamma} \tag{50}$$

and

$$\hat{C}_{,x^I} = \frac{C_{,x^I}}{\int_{\Gamma_d^I} R^I \mathrm{d}\Gamma} \; . \tag{51}$$

Furthermore, for the location updating of the interior control points, a simple linear interpolation scheme is employed by taking the advantage of the coarse design discretization to guarantee the mesh quality. Alternatively, methods such as "shape changing norm" in [46], H^1 gradient method in [69], "traction method" in [70] and [71], and "parametrisation-free" in [72], etc., can also be used for the purpose of mesh quality control. A simple descent algorithm incorporating the penalty-based formulation of sizing constraint is presented in Algorithm 1. For generic constraint optimization problems, well developed optimizers such as the "fmincon" function in Matlab or GCMMA (Globally Convergent Method of Moving Asymptotes) developed by Svanberg [73] can be considered.

7. Results

In the following examples, some general design settings are as follows: the area of the RVE is chosen as 400, i.e., the side length of the square RVE for the smoothed tetra-petals design is 20, while the side length of the hexagonal RVE for the smoothed hexa-petals design is 12.408. The connecting bars between each cells have a fixed width of 1. The Young modulus and Poisson ratio for the constitutive material are set to be 1 and 0.3, respectively.

7.1. Shape optimization of smoothed tetra-petals structure

The design optimization of the tetra-petals structure starts with an initial design that has a fixed interior boundary as shown in Fig. 12(a). The maximal curvature is 2 (equivalent to a radius of 0.5), which results in a reasonably smooth connection with low stress concentration. The gap between two arms is about 1.36. The initial design has a uniform width of 1 (see Fig. 12(b)) and an effective Poisson ratio of −0.6655 along the vertical and horizontal directions. The effective Poisson ratios along different directions are plotted in a polar coordinate system in Fig. 12(c) as proposed in [59,74], which indicates that the effective Poisson ratio of this structure is not isotropic. This design study is termed Case 1 hereinafter.

The tetra-petals structure is optimized with both symmetric and sizing constraints considered. The macro strain of $E = [1, \; 0, \; 0]^{\mathrm{T}}$ is used for the numerical homogenization, with the structure orientation as shown in Fig. 4(d). For practical engineering considerations, the minimal width of the petals arms is set to be 0.5, which is half of its initial size. The optimized shape is shown in Fig. 13(a) with an effective Poisson ratio of −0.878 along both the vertical and horizontal directions. The effective Poisson ratio along different orientations are presented in a polar coordinate system shown in Fig. 13(b). From the polar plot, it is clear that the auxetic behaviour of the optimized design is bi-directionally dominated and has an overall better performance than the initial design. The comparison between the size bounding curve and the initial and optimized designs are plotted in Fig. 13(c), from which it can be seen that the sizing constraint is fully satisfied.

To further evaluate the robustness of the design methodology, we consider two alternative initial designs with maximal curvatures of 4 and 8, termed, respectively, as Case 2 and Case 3. The full model of the initial and optimized designs, as well as the sizing constraint plotted together with the optimized shape of one petal, are depicted in Figs. 14 and 15 for Cases 2 and 3, respectively. Both figures show that the sizing constraint is satisfied. The optimized designs of these three cases are plotted together in Fig. 16(a). The slight variations in the optimized shapes are induced by the different maximum curvatures imposed on the fixed interior boundary and the associated sizing constraint.

Algorithm 1: Descent algorithm with sizing constraint

---

1 **Initialize** ($n = 1$);

2 Choose an initial parent petal design as shown in Fig. 4(c);

3 Define the design control points x^I, $I = 1, \ldots$;

4 Choose a step size $\alpha > 0$ and a tolerance $\delta_1 > 0$ for the main loop;

5 Choose a penalty factor $\beta > 0$ and a tolerance $\delta_2 > 0$ for the sub-loop;

6 Build the full model using the approach presented in Sec 3.1;

7 **Main loop** ($n \geq 1$);

8 **while** $|\Phi^{(n+1)} - \Phi^{(n)}|/\Phi^{(n)} \geq \delta_1$ **do**

9   Solve the homogenization problem to get displacement field $u^{(n)}$ and the objective $\Phi^{(n)}$;

10   Compute adjoint initial strain ε^* and solve the adjoint problem Eq. (28) to get $(u^*)^{(n)}$;

11   Compute the shape gradient $\Phi_{,x^I}$ using Eq. (40);

12   Mapping the shape gradient $\Phi_{,x^I}$ back to the design space shown in Fig. 4(c) using Eq. (41);

13   Evaluate the shape gradient with respect to the design control points of the parent petal using Eq. (42) or Eq. (43);

14   Normalize the shape gradient using Eq. (50);

15   **Sub-loop for constrained minimization**;

16   **Initialize** ($m = 0$);

17   Set penalty factor $\Lambda_C^{(0)} = 0$, the initial gradient $C_{,x^I}^{(0)} = \mathbf{0}$, and $C^{(0)} = -1$;

18   **while** $C < -\delta_2$ **do**

19   **for** $I = 1, \ldots,$ **do**

20   Update the location x^I for sub-iteration m;

21   **if** x^I *located on the left side of the parent petal:* **then**

22                  $\left(x^I\right)^{(n+1,m)} = \left(x^I\right)^{(n)} - \alpha \left(\hat{\Phi}_{,x^I}^{(n)} - \Lambda_C^{(m)} \hat{C}_{,x^I}^{(m)}\right)$;

23   **else if** x^I *located on the right side of the parent petal:* **then**

24   Update the location by mirroring the control points on the left side;

25   **end**

26   **end**

27   Compute $C^{(m)}$ using Eq. (45) and the corresponding gradient $C_{,x^I}^{(m)}$ using Eq. (49);

28   Mapping the shape gradient back to the design space shown in Fig. 4(c) using Eq. (41);

29   Evaluate the shape gradient with respect to the design control points of the parent petal;

30   Normalize the shape gradient using Eq. (50);

31   Update the penalty factor $\Lambda_C^{(m+1)} = \Lambda_C^{(m)} - \beta C^{(m)}$;

32          $m \leftarrow m + 1$;

33   **end**

34   Set $\left(x^I\right)^{(n+1)} = \left(x^I\right)^{(n+1,m)}$, $I = 1, \ldots$;

35   Update the full model of the structure using the approach presented in Sec. 3.1;

36 $n \leftarrow n + 1$;

37 **end**

Nevertheless, the polar plots of the effective Poisson ratio for the three optimized designs in Fig. 16(b) illustrate an almost identical auxetic behaviour. Furthermore, the iteration histories plotted in Fig. 16(c) show a negligible influence of the interior boundary's maximal curvature for these three cases.

To verify the auxetic behaviour of the optimized design for Case 1, a periodic model with 16 by 4 RVEs (unit cells) is loaded vertically with a unit relative displacement between the horizontal surfaces. The vertical surfaces are constrained to remain plane. The analysis is performed in ABAQUS with a resultant relative horizontal displacement of 3.535. The effective negative Poisson ratio of the specimen is therefore, $\bar{\nu} = \varepsilon_2/\varepsilon_1 = -3.535/4 = -0.884$, which agrees with the value of the effective Poisson ratio predicted by the proposed approach. (See Fig. 17.)
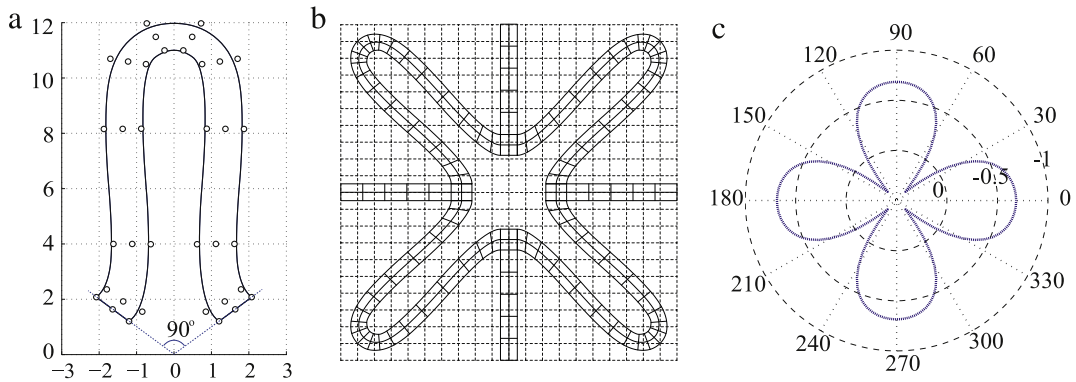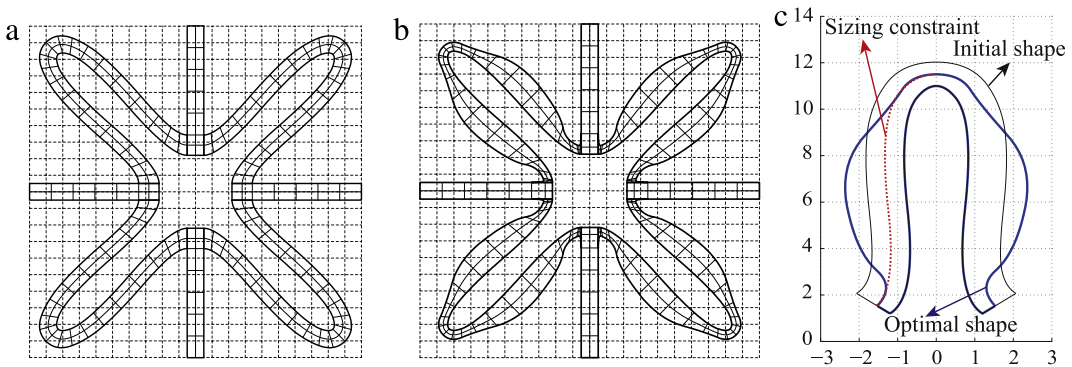
Fig. 12. Case 1: (a) Petal shape and its corresponding control points, (b) the full model, and (c) the polar plot of the effective Poisson ratio for the initial design.
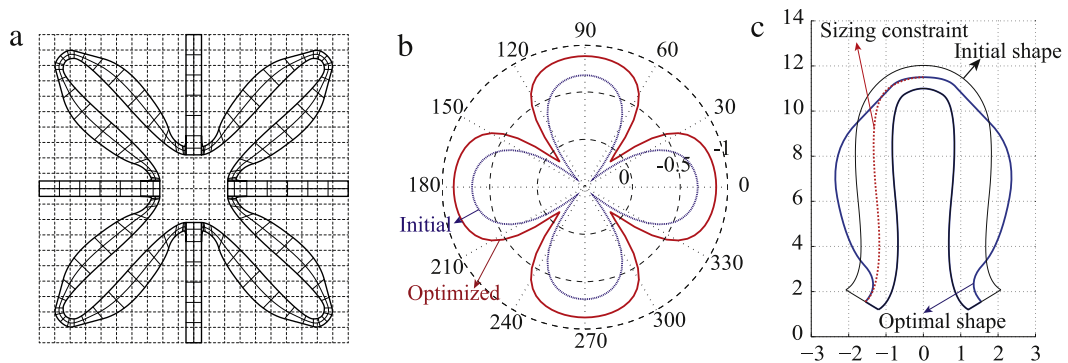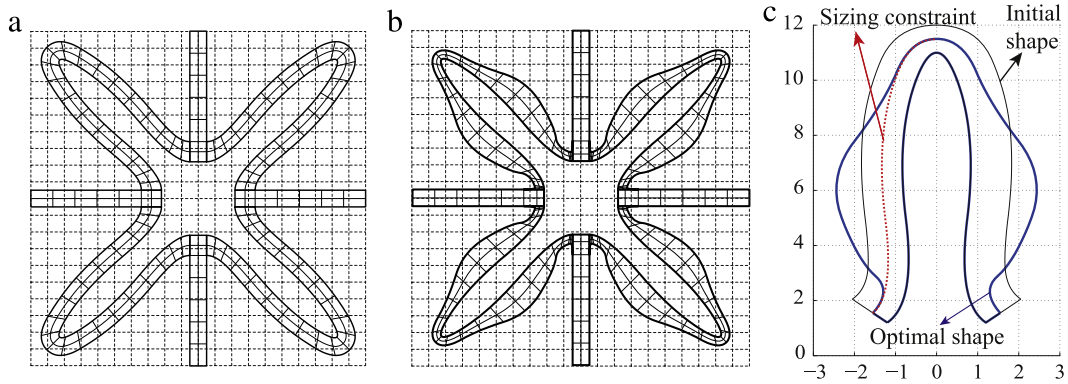

Fig. 13. Case 1: (a) full model of the optimized design. (b) Polar plot of the effective Poisson ratio for the optimized design. (c) Comparison between the size bounding polynomials, the initial and optimized designs.


Fig. 14. Case 2: (a) initial design, (b) optimized design, and (c) the comparison between the size bounding polynomials, the initial and optimized designs.

7.2. Isotropic smoothed hexa-petals auxetic structure design

The design optimization of the smoothed hexa-petals structure starts with an initial design that has a fixed interior boundary shown in Fig. 18. The maximal curvature is 16.5. The gap between two arms is about 0.75. The initial design has a uniform width of 0.8 (Fig. 18(a)) and an effective Poisson ratio of −0.2610. The polar plot of the effective Poisson ratio of hexa-petals structure is shown in Fig. 18(c), which indicates that the effective Poisson ratio is isotropic, as expected due to the 6-fold symmetry of the unit cell.

Fig. 15. Case 3: (a) initial design, (b) optimized design, and (c) the comparison between the size bounding polynomials, the initial and optimized designs.
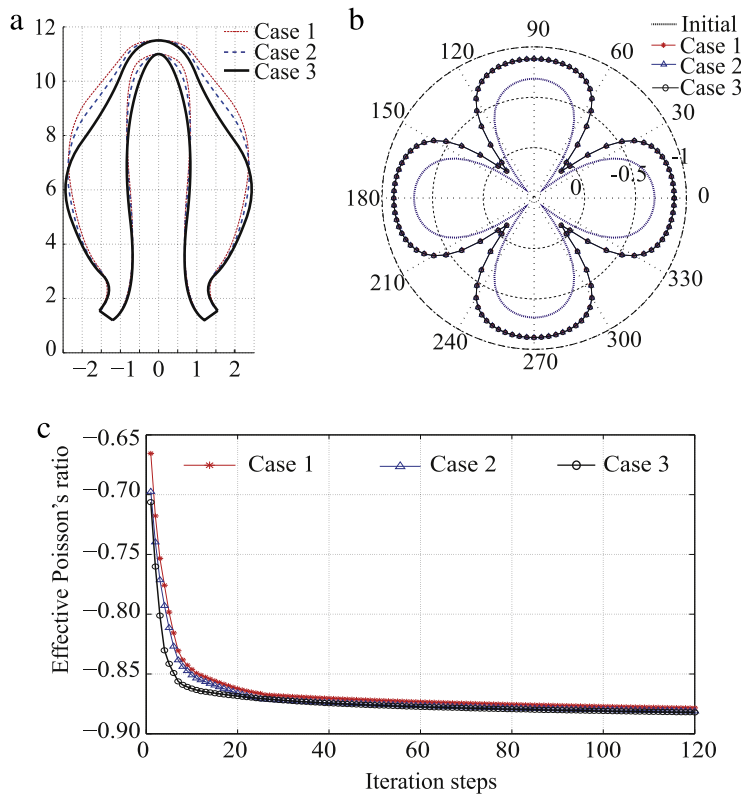

Fig. 16. (a) Optimized shape for the three cases. (b) Polar plots of the effective Poisson ratios for the three optimized designs. (c) Iteration histories of the three design cases.

The hexa-petals structure is optimized with both symmetric and sizing constraints imposed. A macro strain of $E = [1, \ 0, \ 0]^{\mathrm{T}}$ is used for the numerical homogenization with the structure orientation as shown in Fig. 18(b). For practical engineering considerations, the minimal width of the petals arms is set to be 0.5. The optimized shape is shown in Fig. 19(a) with an effective Poisson ratio of -0.431. From the polar plot in Fig. 19(b), it is clear that the auxetic behaviour of the optimized design is isotropic. An isotropic structure design can be very important for the practical engineering applications in cases where the loading direction cannot be determined *a priori*. The comparison between the size bounding curve and the initial and optimized designs are plotted in Fig. 19(c), from which it can be seen the sizing constraint is fully satisfied. The iteration history of the objective function is plotted in Fig. 19(d).
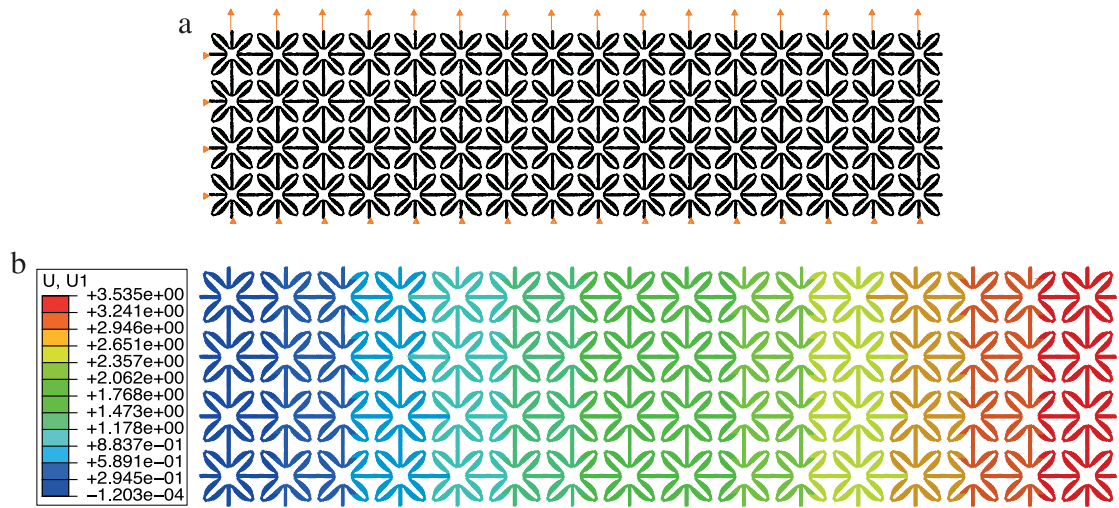
Fig. 17. (a) A periodic model with 16 by 4 units is loaded vertically with a relative unit displacement between the top and bottom surfaces. The vertical surfaces are constrained to remain plane. (b) The horizontal displacement contour plot of the deformed structure.
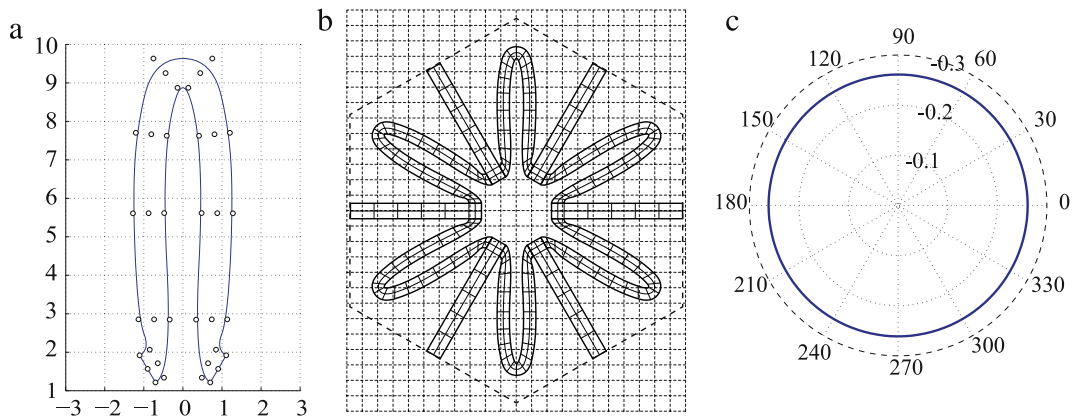

Fig. 18. (a) Petal shape and its corresponding control points, (b) the full model, and (c) the polar plot of the effective Poisson ratio for the initial design.
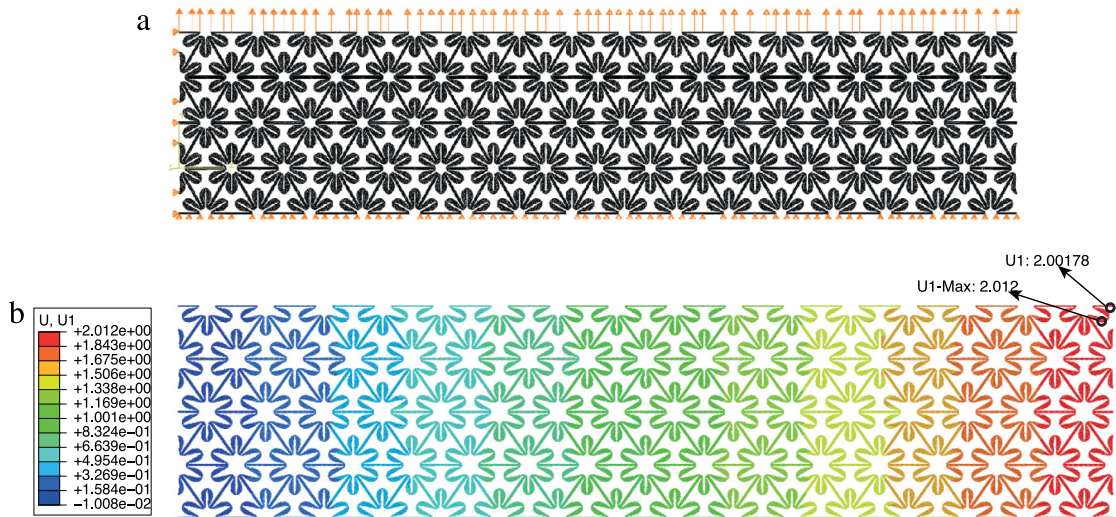
To verify the auxetic behaviour of the optimized design, a periodic model with 16 by 4 units is loaded vertically with a unit relative displacement between the horizontal surfaces. The vertical surfaces are constrained to remain plane. The resultant relative horizontal displacement on the right surface is 2.00178. Given the specimen dimension of 343.86 by 74.448, the effective negative Poisson ratio therefore, is $\bar{\nu} = -\varepsilon_1/\varepsilon_2 = -(2.00178 \times 74.448)/(343.86 \times 1) = -0.433$, which agrees with the predicted value of the effective Poisson ratio reasonably well. (See Fig. 20.)

8. Conclusions

In this paper, we refer to the class of star-shaped designs, upon which a series of smoothed petal auxetics are proposed. These petal auxetic structures utilize smoothed connections to replace the sharp vertices. Shape optimization within an isogeometric framework is performed to design the tetra and hexa petals structures. To impose the sizing constraint, a piece-wise bounding polynomial approach is proposed to overcome the difficulties associated with the non-interpolatory nature of NURBS basis. To the best of our knowledge, an isogeometric shape optimization for auxetics has not been discussed in the literature. We note that the current modelling approach is not able to fully smooth the connection between a straight bar and a petal arm, which is a limitation of $C0$ multi-patch modelling scheme used. The numerical framework presented in this paper can be adapted for a more specific study, e.g.
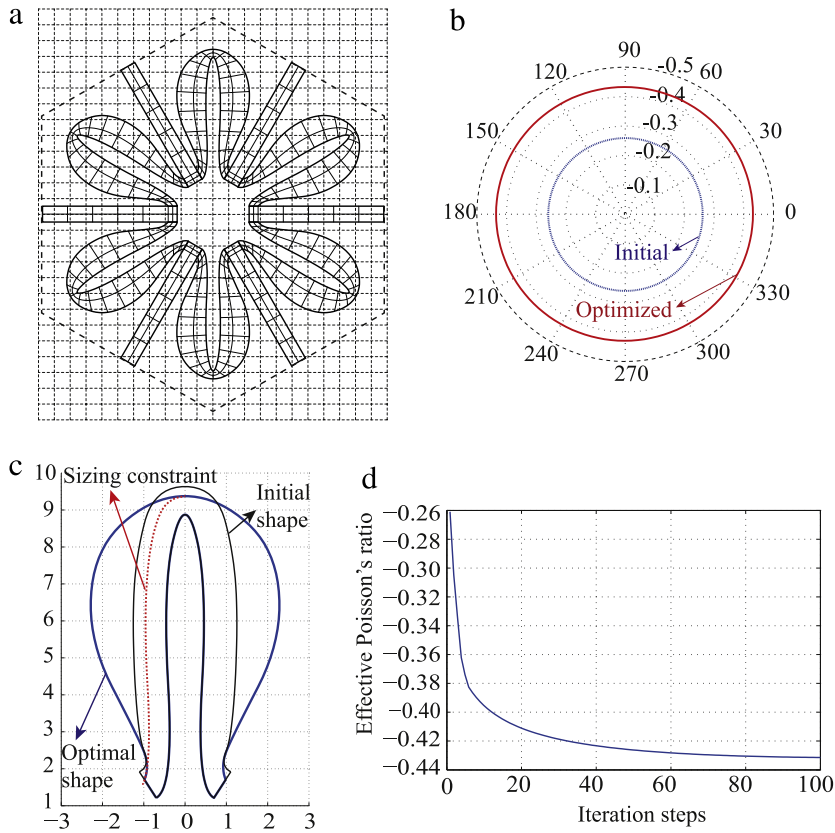
Fig. 19. (a) Full model of the optimized design. (b) Polar plot of the effective Poisson ratio for the optimized design. (c) Comparison between the size bounding polynomials, the initial and optimized designs. (d) Iteration history of the objective function.

Fig. 20. (a) A periodic model with 16 by 4 units is loaded vertically with a unit relative displacement between the top and bottom surfaces. The vertical surfaces are constrained to remain plane. (b) The horizontal displacement contour plot of the deformed structure.

- to obtain a targeted Poisson's ratio as done in [33]. This can be achieved by replacing the objective function $\Phi = \nu$ with $\Psi = (\nu - \check{\nu})^2$, where $\check{\nu}$ is the targeted Poisson's ratio. The material design derivative of Ψ is thus $\mathring{\Psi} = 2(\nu - \check{\nu})\mathring{\Phi}$. For the sensitivity analysis, the loading value of the adjoint problem is changed accordingly by having $2(\nu - \check{\nu})$ in the corresponding terms.
- to impose a minimum stiffness constraint. This can be achieved by using a similar approach as the geometric sizing constraint solved in this work. Alternatively, one can simply incorporate this constraint to a constraint optimizer such as the ones mentioned in Section 6. The sensitivity analysis of the effective stiffness can be derived following the approach in [65].

It is also highlighted that the presented design concepts and numerical framework might be extended possibly for other smooth reference structures. The optimized geometry output can be directly imported to a CAD system for manufacturing without much post-processing operations.

Acknowledgement

References

[1] G.N. Greaves, A. Greer, R. Lakes, T. Rouxel, Poisson's ratio and modern materials, Nature Mater. 10 (11) (2011) 823–837.

[2] W. Yang, Z.-M. Li, W. Shi, B.-H. Xie, M.-B. Yang, Review on auxetic materials, J. Mater. Sci. 39 (10) (2004) 3269–3279.

[3] J. Choi, R. Lakes, Design of a fastener based on negative Poisson's ratio foam, Cell. Polym. 10 (3) (1991) 205–212.

[4] T.-C. Lim, Auxetic Materials and Structures, Springer, 2014.

[5] J.C.Á. Elipe, A.D. Lantada, Comparative study of auxetic geometries by means of computer-aided design and engineering, Smart Mater. Struct. 21 (10) (2012) 105004–105015.

[6] K.K. Saxena, R. Das, E.P. Calius, Three decades of auxetics researchmaterials with negative poisson's ratio: a review, Adv. Energy Mater. 18 (11) (2016) 1847–1870.

[7] H.M. Kolken, A. Zadpoor, Auxetic mechanical metamaterials, RSC Adv. 7 (9) (2017) 5111–5129.

[8] R.F. Almgren, An isotropic three-dimensional structure with poisson's ratio- −1, J. Elasticity 15 (4) (1985) 427–430.

[9] G.W. Milton, Composite materials with poisson's ratios close to -1, J. Mech. Phys. Solids 40 (5) (1992) 1105–1137.

[10] R. Lakes, Foam structures with a negative poisson's Ratio, Science 235 (4792) (1987) 1038–1040.

[11] E. Friis, R. Lakes, J. Park, Negative poisson's ratio polymeric and metallic foams, J. Mater. Sci. 23 (12) (1988) 4406–4414.

[12] K. Evans, Tailoring the negative poisson's ratio, Chem. Ind. (1990) 654–657.

[13] N. Phan-Thien, B. Karihaloo, Materials with negative poissons ratio: a qualitative microstructural model, J. Appl. Mech. 61 (4) (1994) 1001–1004.

[14] S. Babaee, J. Shim, J.C. Weaver, E.R. Chen, N. Patel, K. Bertoldi, 3D soft metamaterials with negative Poisson's ratio, Adv. Mater. 25 (36) (2013) 5044–5049.

[15] O. Sigmund, Materials with prescribed constitutive parameters: an inverse homogenization problem, Int. J. Solids Struct. 31 (17) (1994) 2313–2329.

[16] O. Sigmund, Tailoring materials with prescribed elastic properties, Mech. Mater. 20 (4) (1995) 351–368.

[17] U.D. Larsen, O. Signund, S. Bouwsta, Design and fabrication of compliant micromechanisms and structures with negative poisson's ratio, J. Microelectromech. Syst. 6 (2) (1997) 99–106.

[18] A. Radman, X. Huang, Y. Xie, Topological optimization for the design of microstructures of isotropic cellular materials, Eng. Optim. 45 (11) (2013) 1331–1348.

[19] O. Querin, G. Steven, Y. Xie, Evolutionary structural optimisation (eso) using a bidirectional algorithm, Eng. Comput. 15 (8) (1998) 1031–1048.

[20] X. Huang, Y. Xie, Convergent and mesh-independent solutions for the bi-directional evolutionary structural optimization method, Finite Elem. Anal. Des. 43 (14) (2007) 1039–1049.

[21] X. Huang, M. Xie, Evolutionary Topology Optimization of Continuum Structures: Methods and Applications, Wiley, 2010.

[22] Y. Wang, J. Gao, Z. Luo, T. Brown, N. Zhang, Level-set topology optimization for multimaterial and multifunctional mechanical metamaterials, Eng. Optim. (2016) 1–21.

[23] Y. Wang, Z. Luo, N. Zhang, Z. Kang, Topological shape optimization of microstructural metamaterials using a level set method, Comput. Mater. Sci. 87 (2014) 178–186.

[24] J.A. Sethian, A. Wiegmann, Structural boundary design via level set and immersed interface methods, J. Comput. Phys. 163 (2) (2000) 489–528.

[25] M.Y. Wang, X. Wang, D. Guo, A level set method for structural topology optimization, Comput. Methods Appl. Mech. Engrg. 192 (1) (2003) 227–246.

[26] G. Allaire, F. Jouve, A.-M. Toader, Structural optimization using sensitivity analysis and a level-set method, J. Comput. Phys. 194 (1) (2004) 363–393.

[27] J. Schwerdtfeger, F. Wein, G. Leugering, R. Singer, C. Körner, M. Stingl, F. Schury, Design of auxetic structures via mathematical optimization, Adv. Mater. 23 (22–23) (2011) 2650–2654.

[28] R. Kureta, Y. Kanno, A mixed integer programming approach to designing periodic frame structures with negative poisson's ratio, Optim. Eng. 15 (3) (2014) 773–800.

[29] N.T. Kaminakis, G.E. Stavroulakis, Topology optimization for compliant mechanisms, using evolutionary-hybrid algorithms and application to the design of auxetic materials, Composites B 43 (6) (2012) 2655–2668.

[30] A.A. Javadi, A. Faramarzi, R. Farmani, Design and optimization of microstructure of auxetic materials, Eng. Comput. 29 (3) (2012) 260–276.

[31] E. Horrigan, C.W. Smith, F. Scarpa, N. Gaspar, A.A. Javadi, M. Berger, K.E. Evans, Simulated optimisation of disordered structures with negative poissons ratios, Mech. Mater. 41 (8) (2009) 919–927.

[32] S. Czarnecki, P. Wawruch, The emergence of auxetic material as a result of optimal isotropic design, Phys. Status Solidi b 252 (7) (2015) 1620–1630.

[33] F. Wang, O. Sigmund, J.S. Jensen, Design of materials with prescribed nonlinear properties, J. Mech. Phys. Solids 69 (2014) 156–174.

[34] A. Clausen, F. Wang, J.S. Jensen, O. Sigmund, J.A. Lewis, Topology optimized architectures with programmable Poisson's ratio over large deformations, Adv. Mater. 27 (37) (2015) 5523–5527.

[35] P. Nakshatrala, D. Tortorelli, K. Nakshatrala, Nonlinear structural design using multiscale topology optimization. Part I: Static formulation, Comput. Methods Appl. Mech. Engrg. 261 (2013) 167–176.

[36] L. Xia, P. Breitkopf, Concurrent topology optimization design of material and structure within nonlinear multiscale analysis framework, Comput. Methods Appl. Mech. Engrg. 278 (2014) 524–542.

[37] L. Xia, P. Breitkopf, A reduced multiscale model for nonlinear structural topology optimization, Comput. Methods Appl. Mech. Engrg. 280 (2014) 117–134.

[38] P. Nakshatrala, D. Tortorelli, Nonlinear structural design using multiscale topology optimization. Part II: Transient formulation, Comput. Methods Appl. Mech. Engrg. 304 (2016) 605–618.

[39] S. Nanthakumar, T. Lahmer, X. Zhuang, H.S. Park, T. Rabczuk, Topology optimization of piezoelectric nanostructures, J. Mech. Phys. Solids 94 (2016) 316–335.

[40] P. Theocaris, G. Stavroulakis, P. Panagiotopoulos, Negative poisson's ratios in composites with star-shaped inclusions: a numerical homogenization approach, Arch. Appl. Mech. 67 (4) (1997) 274–286.

[41] J.N. Grima, R. Gatt, A. Alderson, K. Evans, On the potential of connected stars as auxetic systems, Mol. Simul. 31 (13) (2005) 925–935.

[42] V. Carneiro, H. Puga, J. Meireles, Analysis of the geometrical dependence of auxetic behavior in reentrant structures by finite elements, Acta Mech. Sinica 32 (2) (2016) 295–300.

[43] T. J.R. Hughes, J.A. Cottrell, Y. Bazilevs, Isogeometric analysis: CAD, finite elements, NURBS, exact geometry and mesh refinement, Comput. Methods Appl. Mech. Engrg. 194 (39) (2005) 4135–4195.

[44] S. Cho, S.-H. Ha, Isogeometric shape design optimization: exact geometry and enhanced sensitivity, Struct. Multidiscip. Optim. 38 (1) (2009) 53–70.

[45] X. Qian, Full analytical sensitivities in NURBS based isogeometric shape optimization, Comput. Methods Appl. Mech. Engrg. 199 (29) (2010) 2059–2071.

[46] A.P. Nagy, M.M. Abdalla, Z. Gürdal, Isogeometric sizing and shape optimisation of beam structures, Comput. Methods Appl. Mech. Engrg. 199 (17) (2010) 1216–1230.

[47] A.P. Nagy, M.M. Abdalla, Z. Gürdal, Isogeometric design of elastic arches for maximum fundamental frequency, Struct. Multidiscip. Optim. 43 (1) (2011) 135–149.

[48] N.D. Manh, A. Evgrafov, A.R. Gersborg, J. Gravesen, Isogeometric shape optimization of vibrating membranes, Comput. Methods Appl. Mech. Engrg. 200 (13) (2011) 1343–1353.

[49] P. Nørtoft, J. Gravesen, Isogeometric shape optimization in fluid mechanics, Struct. Multidiscip. Optim. 48 (5) (2013) 909–925.

[50] A.P. Nagy, S.T. IJsselmuiden, M.M. Abdalla, Isogeometric design of anisotropic shells: optimal form and material distribution, Comput. Methods Appl. Mech. Engrg. 264 (2013) 145–162.

[51] J. Kiendl, R. Schmidt, R. Wüchner, K.-U. Bletzinger, Isogeometric shape optimization of shells using semi-analytical sensitivity analysis and sensitivity weighting, Comput. Methods Appl. Mech. Engrg. 274 (0) (2014) 148–167.

[52] X. Qian, O. Sigmund, Isogeometric shape optimization of photonic crystals via coons patches, Comput. Methods Appl. Mech. Engrg. 200 (25) (2011) 2237–2255.

[53] B.-U. Park, Y.-D. Seo, O. Sigmund, S.-K. Youn, Shape optimization of the stokes flow problem based on isogeometric analysis, Struct. Multidiscip. Optim. 48 (5) (2013) 965–977.

[54] V. Braibant, C. Fleury, Shape optimal design using b-splines, Comput. Methods Appl. Mech. Engrg. 44 (3) (1984) 247–267.

[55] W.H. Zhang, D. Wang, J.-G. Yang, A parametric mapping method for curve shape optimization on 3d panel structures, Internat. J. Numer. Methods Engrg. 84 (4) (2010) 485–504.

[56] D. Wang, W.-H. Zhang, A bispace parameterization method for shape optimization of thin-walled curved shell structures with openings, Internat. J. Numer. Methods Engrg. 90 (13) (2012) 1598–1617.

[57] S.-Y. Cai, W.H. Zhang, J.H. Zhu, T. Gao, Stress constrained shape and topology optimization with fixed mesh: a b-spline finite cell method combined with level set function, Comput. Methods Appl. Mech. Engrg. 278 (2014) 361–387.

[58] J. Dirrenberger, S. Forest, D. Jeulin, C. Colin, Homogenization of periodic auxetic materials, Procedia Eng. 10 (2011) 1847–1852.

[59] J. Dirrenberger, S. Forest, D. Jeulin, Effective elastic properties of auxetic microstructures: anisotropy and structural applications, Int. J. Mech. Mater. Des. 9 (2013) 21–33.

[60] A. Bacigalupo, M.L. De Bellis, Auxetic anti-tetrachiral materials: equivalent elastic properties and frequency band-gaps, Compos. Struct. 131 (2015) 530–544. http://dx.doi.org/10.1016/j.compstruct.2015.05.039. http://www.sciencedirect.com/science/article/pii/S0263822315004043.

[61] A. Bacigalupo, M. Lepidi, G. Gnecco, L. Gambarotta, Optimal design of auxetic hexachiral metamaterials with local resonators, Smart Mater. Struct. 25 (2016) 054009. http://stacks.iop.org/0964-1726/25/i/=5/a/=054009.

[62] J. Besson, G. Cailletaud, J.-L. Chaboche, S. Forest, M. Blétry, Non–linear mechanics of materials, in: Solid Mechanics and Its Applications, vol. 167, Springer-Verlag, Berlin Heidelberg, 2009.

[63] A. Bacigalupo, L. Gambarotta, Homogenization of periodic hexa- and tetrachiral cellular solids, Compos. Struct. 116 (2014) 461–476. http://dx.doi.org/10.1016/j.compstruct.2014.05.033. http://www.sciencedirect.com/science/article/pii/S0263822314002438.

[64] K.K. Choi, N.-H. Kim, Structural Sensitivity Analysis and Optimization 1: Linear Systems, Springer-Verlag New York, Inc., New York, NY, USA, 2005.

[65] Z.-P. Wang, S. Turteltaub, Isogeometric shape optimization for quasi-static processes, Internat. J. Numer. Methods Engrg. 104 (5) (2015) 347–371.

[66] A. Pressley, Elementary Differential Geometry, Springer, 2010.

[67] Z.-P. Wang, Isogeometric Shape Optimization for Quasi-Static and Transient Problems, Delft University of Technology, Delft, the Netherlands, 2015.

[68] Z.-P. Wang, M. Abdalla, S. Turteltaub, Normalization approaches for the descent search direction in isogeometric shape optimization, Comput. Aided Des. 82 (2017) 68–78.

[69] H. Azegami, S. Fukumoto, T. Aoyama, Shape optimization of continua using NURBS as basis functions, Struct. Multidiscip. Optim. 47 (2) (2013) 247–258.

[70] A.R. Inzarulfaisham, H. Azegami, Solution to boundary shape optimization problem of linear elastic continua with prescribed natural vibration mode shapes, Struct. Multidiscip. Optim. 27 (3) (2004) 210–217.

[71] S. Riehl, J. Friederich, M. Scherer, R. Meske, P. Steinmann, On the discrete variant of the traction method in parameter-free shape optimization, Comput. Methods Appl. Mech. Engrg. (2014).

[72] C. Le, T. Bruns, D. Tortorelli, A gradient-based, parameter-free approach to shape optimization, Comput. Methods Appl. Mech. Engrg. 200 (9) (2011) 985–996.

[73] K. Svanberg, MMA and gcmma, versions september 2007, Optim. Syst. Theory (2007) 104.

[74] J. Dirrenberger, S. Forest, D. Jeulin, Elastoplasticity of auxetic materials, Comput. Mater. Sci. 64 (2012) 57–61.